nature physics

Article

https://doi.org/10.1038/s41567-022-01805-7

Three-state nematicity and magneto-optical Kerr effect in the charge density waves in kagome superconductors

Received: 22 March 2022

Accepted: 23 September 2022

Published online: 7 November 2022

Check for updates

Yishuai Xu[1], Zhuoliang Ni[1], Yizhou Liu[2], Brenden R. Ortiz[3], Qinwen Deng[1], Stephen D. Wilson[3], Binghai Yan[2], Leon Balents[4] & Liang Wu[1]

The kagome lattice provides a fascinating playground to study geometrical frustration, topology and strong correlations. The newly discovered kagome metals AV_3Sb_5 (where A can refer to K, Rb or Cs) exhibit phenomena including topological band structure, symmetry-breaking charge-density waves and superconductivity. Nevertheless, the nature of the symmetry breaking in the charge-density wave phase is not yet clear, despite the fact that it is crucial in order to understand whether the superconductivity is unconventional. In this work, we perform scanning birefringence microscopy on all three members of this family and find that six-fold rotation symmetry is broken at the onset of the charge-density wave transition in all these compounds. We show that the three nematic domains are oriented at 120° to each other and propose that staggered charge-density wave orders with a relative π phase shift between layers is a possibility that can explain these observations. We also perform magneto-optical Kerr effect and circular dichroism measurements. The onset of both signals is at the transition temperature, indicating broken time-reversal symmetry and the existence of the long-sought loop currents in that phase.

The kagome lattice has attracted tremendous research interest for decades because the corner-sharing triangular lattice has inherent geometrical frustrations that host exotic phases such as the quantum spin liquid state[1]. There has been recent interest in the magnetic kagome systems from the perspective of topological electronic structures in magnetic Weyl semimetals such as Mn_3Sn (ref. [2]) and $Co_3Sn_2S_2$ (ref. [3]) and strongly correlated flat bands in Fe_3Sn_2 and FeSn (refs. [4–7]). Strong electronic correlations without magnetism can also lead to exotic phases such as superconductivity with high critical temperature (T_c), but it has often been difficult to reveal different kinds of broken symmetry. Loop currents, originally proposed in cuprate superconductors[8], have also been predicted in the kagome lattice[9–12], but clear evidence has been lacking.

The newly discovered kagome metals AV_3Sb_5 (where A is K, Rb or Cs) are recent examples that host charge density waves (CDWs) below $T_{CDW} \approx 80$–100 K and superconductivity below $T_c \approx 0.9$–2.5 K (refs. [13–24]). In contrast to magnetic kagome materials, AV_3Sb_5 materials do not have detectable local electronic moments[25], but a surprisingly large anomalous Hall effect was reported with a dominant extrinsic skew scattering mechanism[26,27]. An increase of the muon depolarization below the CDW transition temperature in zero-field muon spin resonance measurements on KV_3Sb_5 and CsV_3Sb_5 has been interpreted as evidence of time-reversal symmetry (TRS) breaking, but the onset is not always at T_{CDW} and the muon depolarization is not directly related with the TRS-breaking order parameter[25]. Therefore, direct measurement of the TRS-breaking order parameter at zero field is urgently needed. Another major debate in the community is whether the system has six- or two-fold rotational symmetry in the CDW phase[28–34], and at what temperature the six-fold symmetry breaks. Almost all of the experiments

[1]Department of Physics and Astronomy, University of Pennsylvania, Philadelphia, PA, USA. [2]Department of Condensed Matter Physics, Weizmann Institute of Science, Rehovot, Israel. [3]Materials Department and California Nanosystems Institute, University of California Santa Barbara, Santa Barbara, CA, USA. [4]Kavli Institute for Theoretical Physics, University of California Santa Barbara, Santa Barbara, CA, USA. e-mail: liangwu@sas.upenn.edu

that claimed two-fold symmetry were performed at temperatures far below the CDW transition[28,31,34]. Therefore, whether the two-fold symmetry is directly related to the CDW has not been clear. In this work, we use scanning birefringence microscopy, the magneto-optical Kerr effect and circular dichroism (CD) to reveal that the CDW transition temperature is the onset of six-fold rotational symmetry breaking and TRS breaking. Our micron-scale imaging bridges the gap between nano-scale scanning probes and macroscopic measurements, providing new insight and strong constraints on the interpretation of many results obtained using macroscopic probes.

Three-state nematicity

AV_3Sb_5 (where A is K, Rb or Cs) share a hexagonal crystal structure consisting of a kagome lattice of V atoms coordinated by Sb in the V–Sb sheet stacked between the A sheets (Fig. 1a). Therefore, it is six-fold rotationally symmetric in the normal state above T_{CDW}. In the CDW phase, the 2 × 2 superlattice per layer could form a star-of-David or tri-hexagonal pattern, which retain the six-fold symmetry of the pristine lattice. Nevertheless, a π phase shift between neighbouring layers can reduce the symmetry to two fold (Fig. 1b and Extended Data Fig. 1a). Note that electronically driven nematicity is also two-fold symmetric but with an onset temperature far below T_{CDW} as observed by scanning tunnelling microscopy (STM)[28,31,34].

To study the rotational symmetry in the CDW phase, we perform scanning birefringence measurements as shown in Fig. 1c. Under normal incidence, the change of the polarization, θ_T, depends not only on the out-of-plane magnetization or orbital moment, known as the polar magneto-optical Kerr effect (MOKE), but also on the birefringence term when the rotational symmetry is lower than three fold. We can distinguish two contributions by rotating the polarization of the incident beam,

$$\theta_T = \theta_K + \theta_B \sin(2\phi - \phi_0) \quad (1)$$

where θ_K and θ_B represent the real part of the MOKE and the amplitude of the birefringence and ϕ is the polarization angle of the incident light with respect to the horizontal axis in the laboratory. ϕ_0 is one principal axis of the crystal in the laboratory frame. Note that the 'MOKE', $\theta_K + i\eta$, is actually a complex quantity, and θ_K and η are often called the MOKE and ellipticity, respectively (Methods). Figure 1d shows the temperature-dependent θ_T at different polarizations for RbV_3Sb_5, where the onset of θ_T is at $T_{CDW} \approx 103$ K. As we change the polarization of the incident light, both the sign and the magnitude of θ_T change, with a maximum amplitude of 0.27 mrad at 6 K. Plotting θ_T versus the incident polarization at a constant temperature shows a two-fold symmetric pattern below T_{CDW} (Fig. 1e). In contrast, we observe barely any angle dependence above T_{CDW}, which is consistent with the six-fold symmetry of the kagome lattice. The two-fold symmetric pattern originates from the breaking of the six-fold rotation symmetry due to the formation of the CDW.

We fix the incident polarization and perform a mapping of θ_T with a spatial resolution of 8 μm (Fig. 1f). Three distinct domains marked with red, white and blue are clearly seen in the map. Angle-dependent birefringence measurements in the six selected regions reveal that regions with the same colour have the same polar patterns, (Fig. 1g–i and Extended Data Fig. 1e–g). Between regions with different colour, the polar patterns are rotated by approximately 120° with respect to each other. Figure 1f shows a possible topological defect as observed in $YMnO_3$ (ref. [35]). However, a surface defect exists where the six regions meet, preventing a clear conclusion (Extended Fig. 1b, optical image). Figure 2 shows that KV_3Sb_5 and CsV_3Sb_5 also have three domains, among which the principal axis is also rotated by 120°. A relatively larger deviation from the fitted curve is observed for the Cs compound, which might be due to the slightly uneven surface resulted from cleaving (Extended Data Fig. 2b,c). The temperature dependence of the birefringence of KV_3Sb_5 and CsV_3Sb_5 also shows that the onset of six-fold rotational symmetry breaking is at T_{CDW} (approximately 74 K and 92 K for these two compounds, respectively; Extended Data Fig. 3). In summary, the three nematic domains are a universal feature of the CDW phases in AV_3Sb_5 (where A is Cs, Rb or K).

Polar magneto-optical Kerr effect

In Equation (1), there is a possible isotropic term θ_K coming from the polar MOKE due to TRS breaking. The isotropic MOKE term appears as an offset in the θ_T versus ϕ plot (Figs. 1e and 2b,d and Extended Data Fig. 3b,d). We extract the temperature-dependent MOKE term by fitting the angle dependence using Equation (1). The results for the three compounds are plotted in Fig. 3a–c. RbV_3Sb_5, CsV_3Sb_5 and KV_3Sb_5 show the onset of the MOKE at approximately 103, 92 and 74 K, respectively. Our result agrees with another study on the Cs compound[30]. The fitting also yield one principal axis direction, ϕ_0.

We use a second method to measure the MOKE with denser temperature steps by setting the incident polarization at the principal axis to eliminate the birefringence. The temperature-dependent MOKE obtained by this method for RbV_3Sb_5, CsV_3Sb_5 and KV_3Sb_5 is shown in Fig. 3d–f, clearly showing that the onset of the MOKE signal is universally at T_{CDW} for the AV_3Sb_5 compounds. There is an error bar of ±0.8° in determining the principal axis, but as shown in Extended Data Fig. 4, the temperature-dependent MOKE at $\phi_0 \pm 0.8°$ still exhibits the onset of the MOKE signal at T_{CDW}. Also, a simple estimate assuming that the exact zero birefringence angle is off by 0.8° gives an error bar of 3.7 μrad ($\sin(0.8°) \times 270\ \mu$rad), which is much smaller than the observed MOKE signal.

Note that the two methods shown in Fig. 3 are performed at different locations, which leads to the different magnitude and signs. Different MOKE signs at various regions are also consistent with two TRS-breaking domains. To confirm the consistency between the two methods, we measure the MOKE signal again by the second method in region 2 of RbV_3Sb_5, obtaining data similar to those obtained by method 1 (Extended Data Fig. 1d). Furthermore, thermal cycles at the same location show that the contour of the birefringence domain does not change much (Extended Data Fig. 5). We also find that thermal cycling cannot easily change the sign of the MOKE, in all three compounds, suggesting some unknown pinning mechanism. We point out that the other possible origin of the MOKE is the spin density wave, but there has been no positive evidence of a spin density wave from any measurement. In summary, our MOKE measurements at zero field directly probe the TRS-breaking order parameter and demonstrate that TRS is broken at T_{CDW} for all three AV_3Sb_5 compounds, indicating the existence of the long-sought loop currents in the CDW phases in AV_3Sb_5 (Fig. 3d, inset).

CD

To further confirm TRS breaking in the CDW phase, we measure the CD in these three compounds. Left circularly polarized and right circularly polarized light are normally incident on the sample, and the difference of the reflectivity between them is defined as the CD. The CD measurement is free from the birefringence effect and fitting errors. The measured CD signal can be shown to be proportional to the ellipticity, η, of the MOKE contribution (Methods). Figure 4 shows the CD versus temperature for all three compounds at different spatial locations, clearly revealing an onset of CD at T_{CDW} because the temperature-dependent CD at different spots of the samples splits at T_{CDW}. The locations of these points are shown in the spatial CD mapping in Extended Data Fig. 6. The sharp transition in θ_T is more consistent with a first-order transition in the Cs sample, which is consistent with NMR/nuclear quadrupole resonance measurements[36–38]. The sharp transition is also observed in the birefringence and MOKE measurements (Extended Data Fig. 2a).

Note that CD can also originate from chiral (handed) structures, and there have been theoretical proposals that the CDW on the surface

https://doi.org/10.1038/s41567-022-01805-7

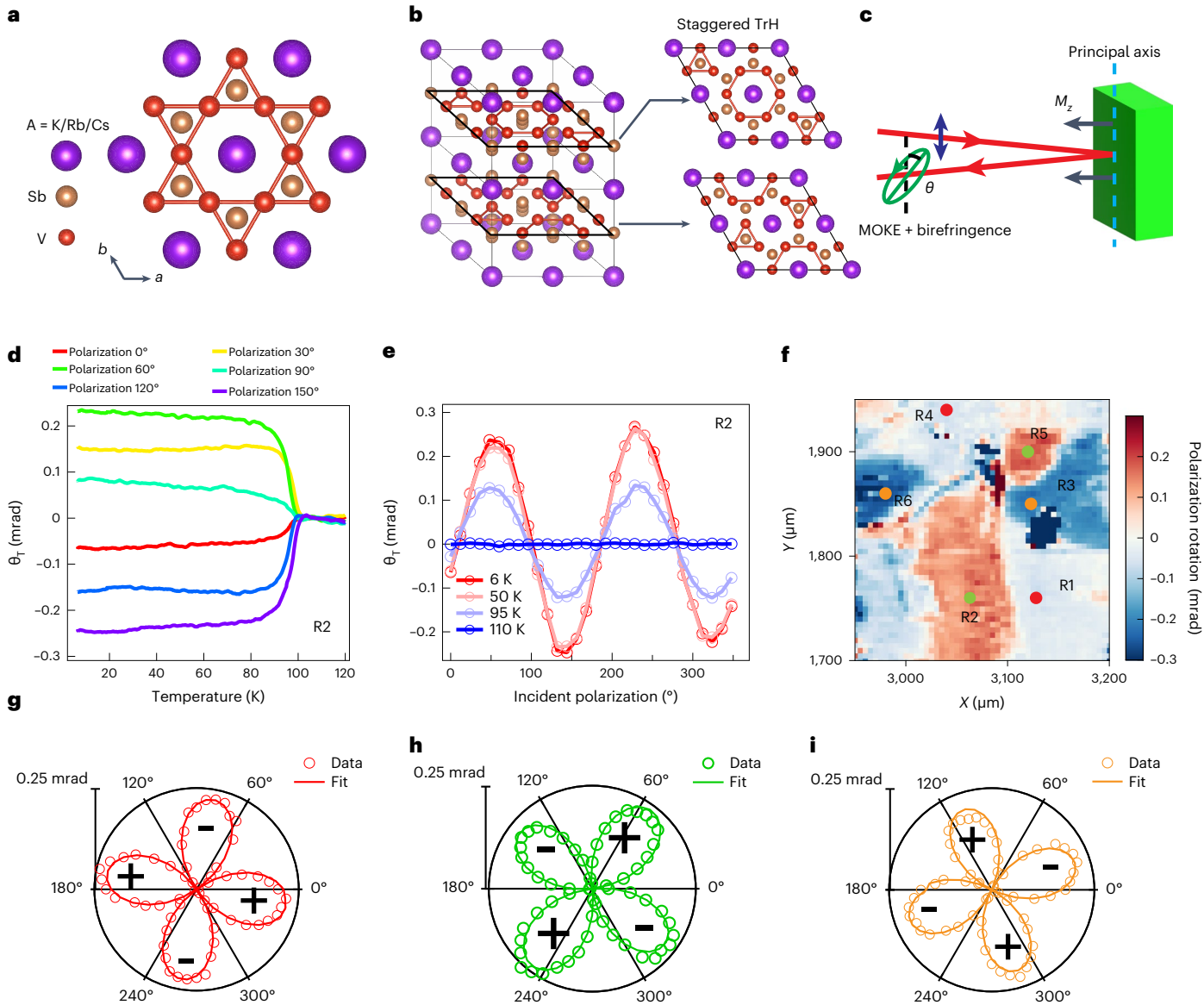

Fig. 1 | Three-state nematic order in RbV_3Sb_5. a, Top view of the kagome lattice structure (a–b plane) of AV_3Sb_5 (where A is K, Rb or Cs). The V_3Sb and K/Rb/Cs layers form the kagome and triangular lattices, respectively. **b**, A 3D crystal structure showing staggered tri-hexagonal (TrH) CDW order. There is a relative phase shift of π between neighbouring in-plane 2 × 2 tri-hexgonal CDW orders. **c**, Schematic showing the change of polarization angle θ_T due to a combination of the magneto-optical Kerr effect and the birefringence effect. M_z is the out-of-plane (z-axis) magnetic moment of sample. **d**, θ_T versus temperature measured at the green spot in region 2 in **f** with different incident polarizations. **e**, θ_T versus incident polarization at different temperatures. The plot is obtained by averaging the data shown in **d** in a window of ±1 K centred around the labelled temperature. **f**, Spatial mapping of θ_T at $T = 6$ K in a RbV_3Sb_5 sample measured at an incident polarization of $\phi = 37.6°$, which corresponds to zero birefringence in R1. Six regions are labelled as R1 to R6, and the red/green/orange spots indicate the positions where the birefringence measurement within each domain are performed. The two dark/blue islands are caused by impurities on the surface (see optical images in Extended data Fig. 1). **g**–**i**, Polar plots of the birefringence patterns at $T = 70$ K at the red dot in region 1 (**g**), green dot in region 2 (**h**) and orange dot in 3 (**i**) marked in **f**. The '+' and '−' symbols show the sign of θ_T.

of AV_3Sb_5 could be chiral if the period along the c axis is four unit cells[10]. As shown in Methods, if both TRS and inversion exist, the CD vanishes. We performed second-harmonic generation (SHG) experiments and observed that the SHG signal is only around 0.2 counts of photons per second under 12 mW incident power (Extended Data Fig. 7). We also do not see any change across the T_{CDW} in SHG. Our observation of AV_3Sb_5 being centrosymmetric agrees with previous studies[29], and our detection sensitivity is much higher[39,40]. Therefore, the presence of CD indicates TRS breaking. Moreover, in CsV_3Sb_5, within the same birefringence domain as shown in Extended Data Fig. 8, we observe two large-area CD domains with opposite sign, providing further strong evidence of TRS breaking. We thus conclude that the onset of CD at the T_{CDW} comes from TRS breaking.

Discussion

Our observation of two-fold symmetry and three-state nematicity just below T_{CDW} is very different from the nematic order observed by STM in CsV_3Sb_5 (refs. [31,34]) and KV_3Sb_5 (ref. [28]), which shows nematic order at temperatures far below T_{CDW}. This difference is probably not just because STM is a surface-sensitive measurement whereas our probe is a bulk measurement with a penetration depth of light of around 50 nm (refs. [41,42]). It could be that the nematicity observed by STM is some kind

https://doi.org/10.1038/s41567-022-01805-7

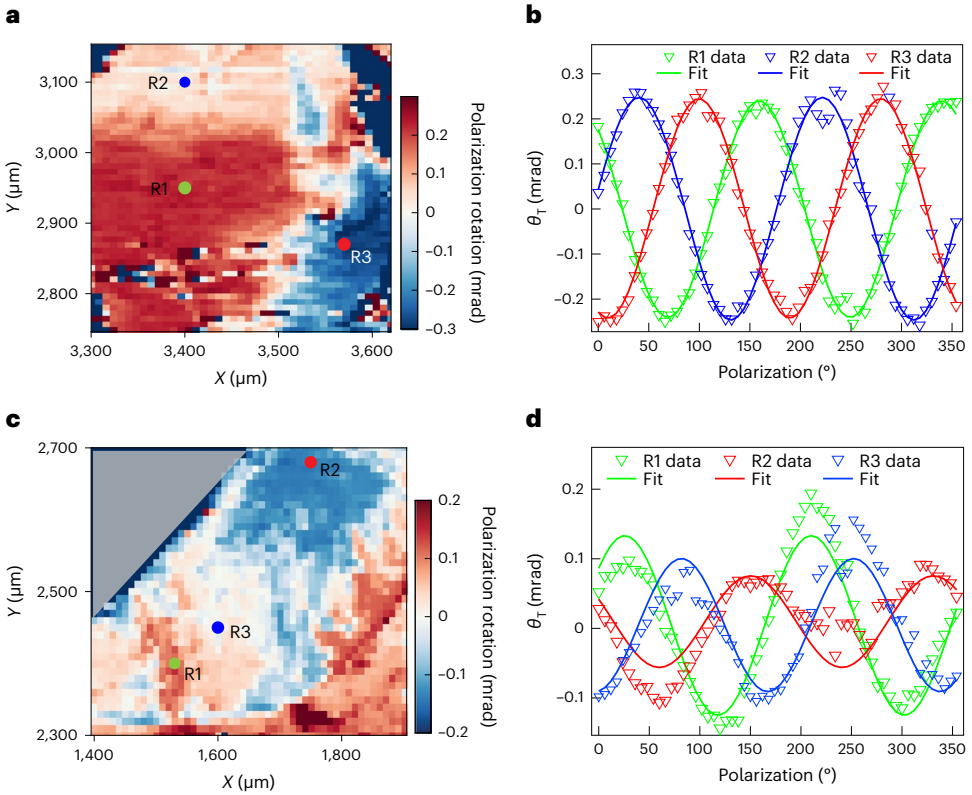

Fig. 2 | Three-state nematic order in KV_3Sb_5 and CsV_3Sb_5. a,**c**, Spatial mapping of θ_T at $T = 6$ K in KV_3Sb_5 (**a**) and CsV_3Sb_5 (**c**) measured at incident polarization of 0° and 46°, respectively. Three domains are labelled R1, R2 and R3. The red/green/blue spots indicate the positions where the birefringence measurements (**b** and **d**) were performed. The grey triangle in **c** indicates region off the sample. **b**,**d**, Birefringence patterns of KV_3Sb_5 (**b**) and CsV_3Sb_5 (**d**) measured at $T = 50$ K and 70 K at green, red and blue dots in region 1, 2 and 3, respectively.

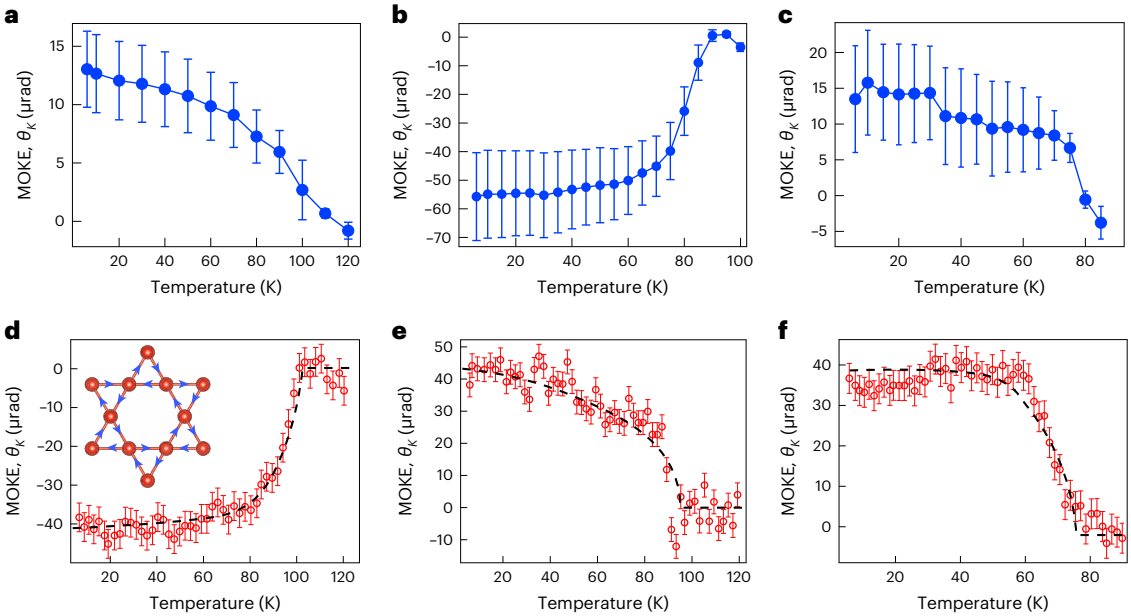

Fig. 3 | MOKE in AV_3Sb_5. a–**c**, Fitted MOKE signal θ_K versus temperature with error bars for the Rb (**a**), Cs (**b**) and K compound (**c**). The data points are the fitted values of θ_K obtained using Equation (1). The error bar is defined as the fitting error of θ_K by Equation (1). The blue curve connects the data points. **d**–**f**, MOKE signal versus temperature measured at the incident angles with zero birefringence for the Rb (**d**), Cs (**e**) and K compound (**f**). The dashed curve is a guide to the eye. The inset in **d** shows the orbital currents (blue arrows) in the kagome lattice. The error bar is 3.7 μrad as defined in the main text, which is larger than the s.d. of the θ_K from 6 to 40 K.

of additional, electronically driven phenomena at low temperature, as proposed recently[28,31,34]. Also, the three domains were not all resolved by STM[28,31,34], probably because of the large domain size. The origin of the two-fold symmetry and three domains observed in our measurement is most likely due to the π phase shift of the stacking between CDW layers (Fig. 1b and Extended Data Fig.1a), because the onset temperature of

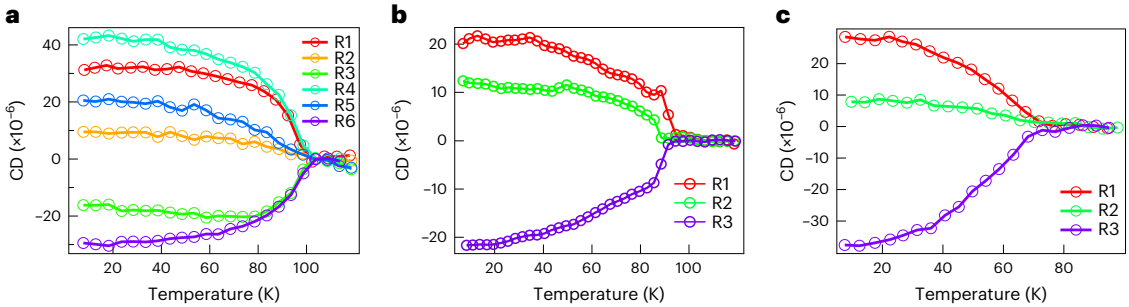

Fig. 4 | CD in AV_3Sb_5. a, CD versus temperature measured at the corresponding spots in regions 1–6 in Extended Data Fig. 6a in RbV_3Sb_5. **b**,**c**, CD versus temperature at the selected spots in regions 1–3 in CsV_3Sb_5 (**b**) and KV_3Sb_5 (**c**) in Extended Data Fig. 6b and 6c, respectively. The error bar is smaller than the symbol size of the data point in **a**–**c**.

birefrigence coincides with T_{CDW} in all three compounds. Many works have proposed different kinds of stacking between CDW layers[29,34,43–46]. Our results show that those without two-fold symmetry are not compatible. The domains we observe are on the order of 100 μm scale, which explains the nematicity observed in transport experiments on macroscopic samples possibly owing to unequal population of three domains[32,33]. Our results add strong constraints on the interpretation of other macroscopic measurements using techniques such as photo-emission, x-ray and optical spectroscopy[29,41–44,46–50].

As predicted in theoretical works[9,10,12,51–53], the interactions between saddle points in the kagome lattice lead to various competing orders such as real and chiral flux CDW orders in AV_3Sb_5. In some parameter regimes, the favoured chiral flux CDW order can also induce real CDW order, leading to a mixture of order parameters. The results from our optical measurements show that both the three-state nematicity and the TRS breaking occur at T_{CDW} in AV_3Sb_5, indicating that these two kinds of symmetry breaking might be intertwined. The TRS breaking is favourable to the chiral flux CDW order with loop currents, which might indicate unconventional superconductivity in these compounds as the superconducting phase develops from the CDW phase. As the MOKE is directly related to the transverse and longitudinal optical conductivity instead of the magnetization, it cannot be used to directly estimate the effective moment. However, it might be worthwhile to point out that the MOKE signal in AV_3Sb_5 is as small as that in Mn_3Sn (ref. [54]). The moment in Mn_3Sn is $0.001\mu_B$, so perhaps the effective moment in AV_3Sb_5 is even smaller as it was not detected by spin susceptibility and muon spin relaxation measurements. Looking forward, we hope that our work will stimulate future work to study the nematicity, the effective moment and TRS breaking in both the CDW and superconducting phases in AV_3Sb_5. The imaging methodologies developed here could also be widely applied to other strongly correlated and topological systems.

Online content

Any methods, additional references, Nature Research reporting summaries, source data, extended data, supplementary information, acknowledgements, peer review information; details of author contributions and competing interests; and statements of data and code availability are available at https://doi.org/10.1038/s41567-022-01805-7.

References

1. Han, T. H. et al. Fractionalized excitations in the spin-liquid state of a kagome-lattice antiferromagnet. *Nature* **492**, 406–410 (2012).
2. Nakatsuji, S., Kiyohara, N. & Higo, T. Large anomalous Hall effect in a non-collinear antiferromagnet at room temperature. *Nature* **527**, 212–215 (2015).
3. Belopolski, I. et al. Discovery of topological Weyl fermion lines and drumhead surface states in a room temperature magnet. *Science* **365**, 1278–1281 (2019).
4. Yin, J. X. et al. Giant and anisotropic many-body spin–orbit tunability in a strongly correlated kagome magnet. *Nature* **562**, 91–95 (2018).
5. Yin, J. X. et al. Negative flat band magnetism in a spin–orbit-coupled correlated kagome magnet. *Nat. Phys.* **15**, 443–448 (2019).
6. Yin, J. X. et al. Quantum-limit Chern topological magnetism in $TbMn_6Sn_6$. *Nature* **583**, 533–536 (2020).
7. Ye, L. et al. Massive Dirac fermions in a ferromagnetic kagome metal. *Nature* **555**, 638–642 (2018).
8. Varma, C. Non-Fermi-liquid states and pairing instability of a general model of copper oxide metals. *Phys. Rev. B* **55**, 14554 (1997).
9. Lin, Y.-P. & Nandkishore, R. M. Complex charge density waves at van Hove singularity on hexagonal lattices: Haldane-model phase diagram and potential realization in the kagome metals AV_3Sb_5 (A=K, Rb, Cs). *Phys. Rev. B* **104**, 045122 (2021).
10. Park, T., Ye, M. & Balents, L. Electronic instabilities of kagome metals: Saddle points and Landau theory. *Phys. Rev. B* **104**, 035142 (2021).
11. Feng, X., Jiang, K., Wang, Z. & Hu, J. Chiral flux phase in the Kagome superconductor AV_3Sb_5. *Sci. Bull.* **66**, 1384–1388 (2021).
12. Denner, M. M., Thomale, R. & Neupert, T. Analysis of charge order in the kagome metal AV_3Sb_5 (A=K, Rb, Cs). *Phys. Rev. Lett.* **127**, 217601 (2021).
13. Ortiz, B. R. et al. New kagome prototype materials: discovery of KV_3Sb_5, RbV_3Sb_5, and CsV_3Sb_5. *Phys. Rev. Mater.* **3**, 094407 (2019).
14. Ortiz, B. R. et al. CsV Sb : a $\mathbb{Z}_2$ topological kagome metal with a superconducting ground state. Phys. Rev. Lett. 125, 247002 (2020).
15. Ortiz, B. R. et al. Superconductivity in the $\mathbb{Z}_2$ kagome metal KV Sb. Phys. Rev. Mater. 5, 034801 (2021).
16. Jiang, Y. X. et al. Unconventional chiral charge order in kagome superconductor KV_3Sb_5. *Nat. Mater.* **20**, 1353–1357 (2021).
17. Xu, H.-S. et al. Multiband superconductivity with sign-preserving order parameter in kagome superconductor CsV_3Sb_5. *Phys. Rev. Lett.* **127**, 187004 (2021).
18. Liu, Z. et al. Charge-density-wave-induced bands renormalization and energy gaps in a kagome superconductor RbV_3Sb_5. *Phys. Rev. X* **11**, 041010 (2021).
19. Shumiya, N. et al. Intrinsic nature of chiral charge order in the kagome superconductor RbV_3Sb_5. *Phys. Rev. B* **104**, 035131 (2021).
20. Wang, Z. et al. Electronic nature of chiral charge order in the kagome superconductor CsV_3Sb_5. *Phys. Rev. B* **104**, 075148 (2021).

21. Wang, Q. et al. Charge density wave orders and enhanced superconductivity under pressure in the kagome metal CsV_3Sb_5. *Adv. Mater.* **33**, 2102813 (2021).
22. Lou, R. et al. Charge-density-wave-induced peak–dip–hump structure and the multiband superconductivity in a kagome superconductor CsV_3Sb_5. *Phys. Rev. Lett.* **128**, 036402 (2022).
23. Chen, H. et al. Roton pair density wave in a strong-coupling kagome superconductor. *Nature* **599**, 222–228 (2021).
24. Yin, Q. et al. Superconductivity and normal-state properties of kagome metal RbV_3Sb_5 single crystals. *Chin. Phys. Lett.* **38**, 037403 (2021).
25. Mielke, C. et al. Time-reversal symmetry-breaking charge order in a kagome superconductor. *Nature* **602**, 245–250 (2022).
26. Yang, S.-Y. et al. Giant, unconventional anomalous hall effect in the metallic frustrated magnet candidate, KV_3Sb_5. *Sci. Adv.* **6**, eabb6003 (2020).
27. Yu, F. H. et al. Concurrence of anomalous hall effect and charge density wave in a superconducting topological kagome metal. *Phys. Rev. B* **104**, L041103 (2021).
28. Li, H. et al. Rotation symmetry breaking in the normal state of a kagome superconductor KV_3Sb_5. *Nat. Phys.* **18**, 265–270 (2022).
29. Ortiz, B. R. et al. Fermi surface mapping and the nature of charge-density-wave order in the kagome superconductor CsV_3Sb_5. *Phys. Rev. X* **11**, 041030 (2021).
30. Wu, Q. et al. The large static and pump-probe Kerr effect with two-fold rotation symmetry in kagome metal CsV_3Sb_5. Preprint at *arXiv:2110.11306* (2021).
31. Zhao, H. et al. Cascade of correlated electron states in the kagome superconductor CsV_3Sb_5. *Nature* **599**, 216–221 (2021).
32. Xiang, Y. et al. Twofold symmetry of c-axis resistivity in topological kagome superconductor CsV_3Sb_5 with in-plane rotating magnetic field. *Nat. Commun.* **12**, 6727 (2021).
33. Ni, S. et al. Anisotropic superconducting properties of kagome metal CsV_3Sb_5. *Chin. Phys. Lett.* **38**, 057403 (2021).
34. Nie, L. et al. Charge-density-wave-driven electronic nematicity in a kagome superconductor. *Nature* **604**, 59–64 (2022).
35. Choi, T. et al. Insulating interlocked ferroelectric and structural antiphase domain walls in multiferroic $YMnO_3$. *Nat. Mater.* **9**, 253–258 (2010).
36. Luo, J. et al. Possible star-of-David pattern charge density wave with additional modulation in the kagome superconductor CsV_3Sb_5. *npj Quantum Mater.* **7**, 30 (2022).
37. Mu, C. et al. s-wave superconductivity in kagome metal CsV_3Sb_5 revealed by $^{121/123}$Sb NQR and ^{51}V NMR measurements. *Chin. Phys. Lett.* **38**, 077402 (2021).
38. Song, D. et al. Orbital ordering and fluctuations in a kagome superconductor CsV_3Sb_5. *Sci. China Phys., Mech. Astron.* **65**, 247462 (2022).
39. Ni, Z. et al. Direct imaging of antiferromagnetic domains and anomalous layer-dependent mirror symmetry breaking in atomically thin $MnPS_3$. *Phys. Rev. Lett.* **127**, 187201 (2021).
40. Ni, Z. et al. Imaging the Néel vector switching in the monolayer antiferromagnet $MnPSe_3$ with strain-controlled Ising order. *Nat. Nanotechnol.* **16**, 782–787 (2021).
41. Zhou, X. et al. Origin of charge density wave in the kagome metal CsV_3Sb_5 as revealed by optical spectroscopy. *Phys. Rev. B* **104**, L041101 (2021).
42. Uykur, E., Ortiz, B. R., Wilson, S. D., Dressel, M. & Tsirlin, A. A. Optical detection of the density-wave instability in the kagome metal KV_3Sb_5. *npj Quantum Mater.* **7**, 16 (2022).
43. Liang, Z. et al. Three-dimensional charge density wave and surface-dependent vortex-core states in a kagome superconductor CsV_3Sb_5. *Phys. Rev. X* **11**, 031026 (2021).
44. Miao, H. et al. Geometry of the charge density wave in the kagome metal AV_3Sb_5. *Phys. Rev. B* **104**, 195132 (2021).
45. Ratcliff, N., Hallett, L., Ortiz, B. R., Wilson, S. D. & Harter, J. W. Coherent phonon spectroscopy and interlayer modulation of charge density wave order in the kagome metal CsV_3Sb_5. *Phys. Rev. Mater.* **5**, L111801 (2021).
46. Li, H. et al. Observation of unconventional charge density wave without acoustic phonon anomaly in kagome superconductors AV_3Sb_5 (A = Rb, Cs). *Phys. Rev. X* **11**, 031050 (2021).
47. Kang, M. et al. Twofold van Hove singularity and origin of charge order in topological kagome superconductor CsV_3Sb_5. *Nat. Phys.* **18**, 301–308 (2022).
48. Luo, H. et al. Electronic nature of charge density wave and electron–phonon coupling in kagome superconductor KV_3Sb_5. *Nat. Commun.* **13**, 273 (2022).
49. Nakayama, K. et al. Carrier injection and manipulation of charge-density wave in kagome superconductor CsV_3Sb_5. *Phys. Rev. X* **12**, 011001 (2022).
50. Nakayama, K. et al. Multiple energy scales and anisotropic energy gap in the charge-density-wave phase of the kagome superconductor CsV_3Sb_5. *Phys. Rev. B* **104**, L161112 (2021).
51. Kiesel, M. L., Platt, C. & Thomale, R. Unconventional Fermi surface instabilities in the kagome Hubbard model. *Phys. Rev. Lett.* **110**, 126405 (2013).
52. Christensen, M., Birol, T., Andersen, B. & Fernandes, R. Theory of the charge density wave in AV_3Sb_5 kagome metals. *Phys. Rev. B* **104**, 214513 (2021).
53. Tan, H., Liu, Y., Wang, Z. & Yan, B. Charge density waves and electronic properties of superconducting kagome metals. *Phys. Rev. Lett.* **127**, 046401 (2021).
54. Higo, T. et al. Large magneto-optical Kerr effect and imaging of magnetic octupole domains in an antiferromagnetic metal. *Nat. Photonics* **12**, 73–78 (2018).

Methods

Sample growth method

Single crystals of CsV_3Sb_5, RbV_3Sb_5 and KV_3Sb_5 were synthesized from Cs (liquid, 99.98%; Alfa), Rb (liquid, 99.75%; Alfa), K (metal, 99.95%; Alfa), V (powder, 99.9%; Sigma) and Sb (shot, 99.999%; Alfa). As-received vanadium powder was purified in-house to remove residual oxides. Due to the extreme reactivity of elemental alkalis, all further preparation of AV_3Sb_5 crystals was performed in an argon glove box with oxygen and moisture levels below 0.5 ppm. AV_3Sb_5 single crystals were synthesized using the self-flux method. Elemental reagents were milled in a pre-seasoned tungsten carbide vial to form a composition of 50 at.% $A_{0.4}Sb_{0.6}$ and approximately 50 at.% VSb_2. Excess antimony can be added to the flux to suppress volatility if needed. The fluxes were loaded into alumina crucibles and sealed within stainless-steel jackets. The samples were heated to 1000 °C at 250 °C h^{-1} and soaked there for 24 h. The samples were subsequently cooled to 900 °C at 100 °C h^{-1} and then further to 500 °C at 1 °C h^{-1}. Once cooled, the crystals are recovered mechanically. Crystals are hexagonal flakes with brilliant metallic lustre. The elemental composition of the crystals was assessed using energy-dispersive x-ray spectroscopy using a APREOC scanning electron microscope.

Birefringence and MOKE measurements

Laser pulses from a Ti:sapphire oscillator with 800 nm centre wavelength, 80 MHz repetition rate and 50 fs pulse duration were used to measure the change of the polarization angle. To measure the change of the polarization angle without rotating the sample, a half-wave plate (HWP) is placed immediately in front of the sample and between it and the cube beam splitter. Both the incident and reflected light go through the HWP, thus the polarization change due to the HWP is cancelled. The net change of the polarization comes purely from the sample itself. By rotating the HWP, we can measure the change of polarization θ_T for different incident polarizations. The background from the HWP is calibrated at a temperature of around 20 K above T_{CDW}. The optical set-up for the birefringence measurement is shown in Extended Data Fig. 9a. All of the scanning imaging experiments in this work were performed by fixing the laser beam spot but moving the sample using Attocube *xyz* positioners.

In the following derivation, we show how the birefringence and the MOKE signal can be distinguished by rotating the HWP while keeping the beam at the same spot. The Jones matrices for the polarizer at 45° and 0°, the photo-elastic modulator (PEM), the HWP as a function of α (the angle between the fast axis of the HWP and the horizontal axis of the laboratory) and the mirror are

$$P(45) = \frac{1}{2}\begin{bmatrix} 1 & 1 \\ 1 & 1 \end{bmatrix}$$

$$P(0) = \begin{bmatrix} 1 & 0 \\ 0 & 0 \end{bmatrix}$$

$$\mathrm{HWP}(\alpha) = \begin{bmatrix} \cos(2\alpha) & \sin(2\alpha) \\ \sin(2\alpha) & -\cos(2\alpha) \end{bmatrix},$$

$$\mathrm{PEM} = \begin{bmatrix} 1 & 0 \\ 0 & e^{i\tau} \end{bmatrix}$$

$$M = \begin{bmatrix} 1 & 0 \\ 0 & -1 \end{bmatrix}$$

where τ is the phase retardation applied by the PEM. The rotation matrix is

$$R(\beta) = \begin{bmatrix} \cos(\beta) & -\sin(\beta) \\ \sin(\beta) & \cos(\beta) \end{bmatrix}$$

where β is the angle of rotation. For a sample that exhibits both the birefringence and MOKE effects, we can use the following Jones matrix to represent the sample (ignoring the higher-order term):

$$S(\theta) = \begin{bmatrix} 1-\sin(\theta)^2\Delta & \frac{\Delta\sin(2\theta)}{2} - c \\ \frac{\Delta\sin(2\theta)}{2} + c & 1-\cos(\theta)^2\Delta \end{bmatrix}, \quad (2)$$

where θ is the angle between the fast axis and the polarization of the incident light, $\Delta = \delta + i\kappa$ is the complex birefringence term, and $c = \theta_K + i\eta$ comes from the MOKE effect and is also a complex number. The output light O measured at the photo-detector can be calculated as

$$\begin{aligned} O &= P(0)\,\mathrm{HWP}(\pi-\alpha)\,MS(\theta)\,\mathrm{HWP}(\alpha) \\ &\quad \mathrm{PEM}\,P(45)\begin{bmatrix} E \\ 0 \end{bmatrix} \\ &= E\begin{bmatrix} \frac{\Delta\cos(4\alpha-2\theta)}{4} + \frac{ce^{ri}}{2} - \frac{\Delta}{4} + \frac{\Delta e^{ri}\sin(4\alpha-2\theta)}{4} + \frac{1}{2} \\ 0 \end{bmatrix}. \end{aligned}$$

We see that the above expression only depends on the angle difference term $4\alpha - 2\theta$, thus we can set $\theta = 0$ without affecting the final results. The intensity measured at the photo-detector is (ignoring the higher-order terms)

$$\begin{aligned} I(t) &= |O|^2 = E^2\left[\sin(\tau)\left(-\frac{\eta}{2} - \frac{\kappa\sin(4\alpha)}{4}\right)\right. \\ &\quad + \cos(\tau)\left(\frac{\theta_K}{2} + \frac{\delta\sin(4\alpha)}{4}\right) + \frac{\delta\cos(4\alpha)}{4} - \frac{\delta}{4}. \\ &\quad \left. + \frac{1}{4}\right] + \mathcal{O}(h) \end{aligned}$$

Setting $\tau = \tau_0\sin(\omega t)$ and using the Fourier decomposition of $\cos(\tau(t))$ and $\sin(\tau(t))$, we obtain the relation

$$\begin{aligned} I(t) &= E^2\left[\frac{\delta\cos(4\alpha)}{4} - \frac{\delta}{4} + \frac{1}{4}\right. \\ &\quad + 2J_1(\tau_0)\sin(\omega t)\left(-\frac{\eta}{2} - \frac{\kappa\sin(4\alpha)}{4}\right) \\ &\quad \left. + (J_0(\tau_0) + 2J_2(\tau_0)\cos(2\omega t))\left(\frac{\theta_K}{2} + \frac{\delta\sin(4\alpha)}{4}\right)\right] \\ &\quad + \mathcal{O}(h) \end{aligned}$$

The 1*f*, 2*f* and direct-current (DC) components of the signal are

$$\begin{aligned} I(1f) &= E^2 2J_1(\tau_0)\left(-\frac{\eta}{2} - \frac{\kappa\sin(4\alpha)}{4}\right)\sin(\omega t), \\ I(2f) &= E^2 2J_2(\tau_0)\left(\frac{\theta_K}{2} + \frac{\delta\sin(4\alpha)}{4}\right)\cos(2\omega t), \\ I(\mathrm{DC}) &= E^2\left[\frac{\delta\cos(4\alpha)}{4} - \frac{\delta}{4} + \frac{1}{4}\right. \\ &\quad \left. + J_0(\tau_0)\left(\frac{\theta_K}{2} + \frac{\delta\sin(4\alpha)}{4}\right)\right]. \end{aligned}$$

We can set $\tau_0 = 2.405$, which is the zero point for the J_0 Bessel function. Since both δ and θ_K are very small, we can approximate the DC term by $I(\mathrm{DC}) = E^2/4$. Furthermore, lock-in measures the r.m.s. of the signal, so we have the relations

$$\frac{I_{\mathrm{lock}}(1f)}{I_{\mathrm{lock}}(\mathrm{DC})} = \frac{4J_1(\tau_0)}{\sqrt{2}}\left(-\eta - \frac{\kappa\sin(4\alpha)}{2}\right), \quad (3)$$

$$\frac{I_{\mathrm{lock}}(2f)}{I_{\mathrm{lock}}(\mathrm{DC})} = \frac{4J_2(\tau_0)}{\sqrt{2}}\left(\theta_K + \frac{\delta\sin(4\alpha)}{2}\right). \quad (4)$$

Finally, noting that the polarization ϕ of the incident light changes twice as much as the change of the HWP angle $\phi = 2\alpha$, we have the relations

$$-\eta - \frac{\kappa \sin(2\phi)}{2} = \frac{\sqrt{2}}{4J_1(\tau_0)} \frac{I_{\text{lock}}(1f)}{I_{\text{lock}}(\text{DC})}, \tag{5}$$

$$\theta_{\text{K}} + \frac{\delta \sin(2\phi)}{2} = \frac{\sqrt{2}}{4J_2(\tau_0)} \frac{I_{\text{lock}}(2f)}{I_{\text{lock}}(\text{DC})}. \tag{6}$$

We can see that the change of the polarization angle in Equation (6) has a constant MOKE term θ_{K} and a ϕ-dependent birefringence term $\delta \sin(2\phi)/2$.

CD measurement

The optical set-up for the CD measurement is shown in Extended Data Fig. 9b. The alternating, left circularly polarized and right circularly polarized light generated by the PEM are reflected off the sample, and the difference between their intensity (the CD) is measured by a photo-detector connected to a lock-in analyser. The PEM modulates the incident light between left circularly and right circularly polarized at a frequency of $f = 42$ kHz. Both the 1f and DC component are extracted from the measured signal, and the CD of the sample is proportional to $I(1f)/I(\text{DC})$.

Similar to the previous derivation, we can write out the Jones matrix for the CD. The output light after going through the 45° polarizer, the PEM and the sample is

$$\begin{aligned} O &= MS(\theta)\,\text{PEM}\,P(45)\begin{bmatrix} E \\ 0 \end{bmatrix} \\ &= E\begin{bmatrix} -\frac{\Delta \sin(\theta)^2}{2} - \frac{e^{ri}\left(c - \frac{\Delta \sin(2\theta)}{2}\right)}{2} + \frac{1}{2} \\ -\frac{c}{2} + \frac{e^{ri}\left(\Delta \cos(\theta)^2 - 1\right)}{2} - \frac{\Delta \sin(2\theta)}{4} \end{bmatrix}. \end{aligned}$$

The intensity measured by the photo-detector is

$$\begin{aligned} I(t) &= E^2\left(\sin(\tau)\,\eta + \cos(\tau)\,\frac{\delta \sin(2\theta)}{2} - \frac{\delta}{2} + \frac{1}{2}\right) \\ &\quad + \mathcal{O}(h) \\ &= E^2\left[\frac{1}{2} - \frac{\delta}{2} + 2J_1(\tau_0)\sin(\omega t)\eta \right. \\ &\quad \left. + \left(J_0(\tau_0) + 2J_2(\tau_0)\cos(2\omega t)\right)\frac{\delta \sin(2\theta)}{2}\right] \\ &\quad + \mathcal{O}(h) \end{aligned},$$

where $\tau_0 = \frac{\pi}{2}$. To obtain I_{CD}, we measure the ratio between the 1f and DC component, which is equal to

$$I_{\text{CD}} = \frac{I_{\text{lock}}(1f)}{I_{\text{lock}}(\text{DC})} = 2\sqrt{2}J_1\left(\frac{\pi}{2}\right)\eta. \tag{7}$$

We see from Equation (7) that the CD signal does not depend on the sample orientation (θ), as expected, and is only related to the ellipticity η term from the MOKE effect.

In our optical set-up, we used a 50:50 non-polarizing cube in between the PEM and the objective to collect the signal. The non-polarizing cube has different transmission coefficients for s- and p-polarized light across the 750–850 nm wavelength range of our pulsed laser. To account for this s and p transmission difference and rule out its effect on the CD signal, we can add in the Jones matrix for the cube (C) into the CD derivation:

$$C = \begin{bmatrix} \sqrt{T_p} & 0 \\ 0 & \sqrt{T_s} \end{bmatrix}$$

where T_s and T_p are the transmission coefficients for s- and p-polarized light. The output light in this case is

$$O = \begin{bmatrix} \sqrt{1-T_p} & 0 \\ 0 & \sqrt{1-T_s} \end{bmatrix} MS(\theta) \begin{bmatrix} \sqrt{T_p} & 0 \\ 0 & \sqrt{T_s} \end{bmatrix} \cdot \text{PEM}\,P(45)\begin{bmatrix} E \\ 0 \end{bmatrix}$$

The intensity measured by the photo-detector is

$$\begin{aligned} I(t) &= -2J_1(\tau_0)\sin(\omega t)\sqrt{T_pT_s}\left[\frac{(T_s+T_p-2)\eta}{2}\right. \\ &\quad \left. + \frac{(T_s-T_p)\kappa \sin(2\theta)}{4}\right] - \left(J_0(\tau_0) + 2J_2(\tau_0)\cos(\omega t)\right) \\ &\quad \sqrt{T_pT_s}\left[\frac{(T_s-T_p)\theta_K}{2} + \frac{(T_p+T_s-2)\delta \sin(2\theta)}{4}\right] \\ &\quad + \frac{T_s+T_p-T_s^2-T_p^2}{4} + \frac{\delta}{2}\left[T_s^2 - T_s + T_s\sin^2(\theta)\right. \\ &\quad \left. - T_p\sin^2(\theta) - T_s^2\sin^2(\theta) + T_p^2\sin(\theta)\right] + \mathcal{O}(h) \end{aligned},$$

where $\tau_0 = \frac{\pi}{2}$. Now, the CD signal becomes

$$\begin{aligned} I_{\text{CD}} &= \frac{I_{\text{lock}}(1f)}{I_{\text{lock}}(\text{DC})} = \frac{J_1(\tau_0)\sqrt{2T_pT_s}}{T_s+T_p-T_s^2-T_p^2} \\ &\quad \left[2(T_s+T_p-2)\eta + (T_s-T_p)\kappa \sin(2\theta)\right] \end{aligned}.$$

We see now that there is a birefringence correction term in the CD signal as follows:

$$I_{\text{bire}} = \frac{J_1(\eta_0)\sqrt{2T_pT_s}(T_s-T_p)\kappa \sin(2\theta)}{T_s+T_p-T_s^2-T_p^2}. \tag{8}$$

This correction term is proportional to the product of κ and the difference in the transmission coefficients $T_s - T_p$. Given the specification of the non-polarized cube $|T_s - T_p| \approx 10^{-2}$, we can estimate the magnitude of such correction to be

$$I_{\text{bire}} \propto \kappa \cdot (T_s - T_p) = 10^{-4} \times 10^{-2} = 10^{-6}. \tag{9}$$

The birefringence correction is one order of magnitude smaller than the CD signal of the samples and can thus be ignored in our measurement.

CD theory

We derive the general CD effect and discuss the consequences of TRS-breaking and crystal symmetry-breaking on CD. According to Fermi's Golden Rule, the absorption rate of circular light with helicity $\sigma_{\pm}$ is

$$I(\sigma_{\pm}) = \frac{2\pi}{\hbar}\sum_{c,v}|\langle c|H'|v\rangle|^2\delta(E_c - E_v - \hbar\omega), \tag{10}$$

where v and c refer to valance and conduction band states, respectively, and $\hbar\omega$ is the photon energy. H' is the interaction Hamiltonian, whose expression is given by

$$H' = -e\mathbf{E}\cdot\mathbf{r} - \mathbf{m}\cdot\mathbf{B}. \tag{11}$$

The two terms on the right-hand side of Equation (11) correspond to electric and magnetic dipole interactions, respectively. The magnetic dipole term is usually much weaker than the electric dipole term. However, the magnetic dipole cannot be ignored for CD in time-reversal-invariant systems where the electric dipole contribution vanishes, as illustrated below.

For a helical photon $\sigma_{\pm}$, the electric and magnetic field is

$$\mathbf{E} = E_0(1, \pm \mathrm{i}, 0) \quad , \quad \mathbf{B} = \frac{E_0}{c}(\mp \mathrm{i}, 1, 0), \tag{12}$$

so that the interaction matrix element is

$$|\langle c|H'_{\pm}|v\rangle|^2 = |E_0|^2 |\langle c|er_{\pm} \mp \mathrm{i}\frac{m_{\pm}}{c}|v\rangle|^2, \tag{13}$$

where $r_{\pm} = x \pm \mathrm{i}y$ and $m_{\pm} = m_x \pm \mathrm{i}m_y$. Therefore, the CD is

$$\begin{aligned} I(\sigma_+) - I(\sigma_-) &\propto |\langle c|H'_+|v\rangle|^2 - |\langle c|H'_-|v\rangle|^2 \\ =2\mathrm{Im}\Bigg[& \underbrace{e^2\langle v|x|c\rangle\langle c|y|v\rangle}_{①} \\ & + \underbrace{\frac{e}{c}\langle v|m_x|c\rangle\langle c|x|v\rangle + \frac{e}{c}\langle v|m_y|c\rangle\langle c|y|v\rangle}_{②} \\ & + \underbrace{\frac{1}{c^2}\langle v|m_y|c\rangle\langle c|m_x|v\rangle}_{③}\Bigg]. \end{aligned} \tag{14}$$

In Equation (14), ① comes from electric dipole, ② originates in both electric and magnetic dipoles, and ③ comes from merely magnetic dipole interactions. The term ③ is usually ignored since it is too small compared with ① and ②.

Term ① is the Berry curvature between the valance band v and conduction band c. It is even under inversion symmetry but odd under TRS. It is usually called the magnetic CD in literature. Term ② is even under TRS but odd under mirror reflection or inversion, because, for example, $\langle v|m_x|c\rangle\langle c|x|v\rangle$ is odd under $x/y \to -x/-y$ reflection or $(x, y, z) \to (-x, -y, -z)$ inversion. Therefore, if TRS is broken, both ① and ② are nonzero. If TRS is conserved, only term ② can appear in a chiral material. If both TRS and inversion symmetry exist, the CD effect vanishes. In the case of inversion and/or mirror symmetries in the material, the CD effect due to term ① indicates TRS-breaking.

Data availability

All data needed to evaluate the conclusions in the paper are present in the paper and the extended data figures. Additional data related to this paper can be requested from the authors. Source data are provided with this paper.

Acknowledgements

We thank C. Varma, Z. Wang and I. Zeljkovic for helpful discussions. This project is mainly supported by L.W.'s startup package at the University of Pennsylvania. The development of the imaging systems was sponsored by the Army Research Office and was accomplished under grants no. W911NF-21-1-0131, W911NF-20-2-0166 and W911NF-19-1-0342, and the Vice Provost for Research University Research Foundation. Y.X. is also partially supported by the NSF EAGER grant via the CMMT programme (DMR-2132591), a seed grant from NSF-funded Penn MRSEC (DMR-1720530) and the Gordon and Betty Moore Foundation's EPiQS Initiative, and grant GBMF9212 to L.W.. Z.N. acknowledges support from the Vagelos Institute of Energy Science and Technology graduate fellowship and the Dissertation Completion Fellowship at the University of Pennsylvania. B.R.O. and S.D.W. acknowledge support via the UC Santa Barbara NSF Quantum Foundry funded via the Q-AMASE-i program under award DMR-1906325. Q.D. is partially supported by the NSF EPM program under grant no. DMR-2213891. B.Y. acknowledges funding from the European Research Council (ERC) under the European Union's Horizon 2020 research and innovation programme (ERC Consolidator Grant 'NonlinearTopo', no. 815869). L.B. is supported by the NSF CMMT program under grant no. DMR-2116515. L.W. acknowledges the support by the Air Force Office of Scientific Research under award no. FA9550-22-1-0410.

Author contributions

L.W. conceived and supervised the project. Y.X. performed the experiments and analysed the data with Z.N., Q.D. and L.W.. Y.L. and B.Y. performed the CD symmetry analysis. B.R.O. and S.D.W. grew the crystals. L.W., Y.X., S.D.W., B.Y. and L.B. discussed and interpreted the data. L.W. and Y.X. wrote the manuscript with input from all authors. All authors edited the manuscript.

Competing interests

The authors declare no competing financial interests.

Additional information

Extended data is available for this paper at https://doi.org/10.1038/s41567-022-01805-7.

Supplementary information The online version contains supplementary material available at https://doi.org/10.1038/s41567-022-01805-7.

Correspondence and requests for materials should be addressed to Liang Wu.

Peer review information *Nature Physics* thanks Turan Birol, Hu Miao and Luyi Yang for their contribution to the peer review of this work.

https://doi.org/10.1038/s41567-022-01805-7

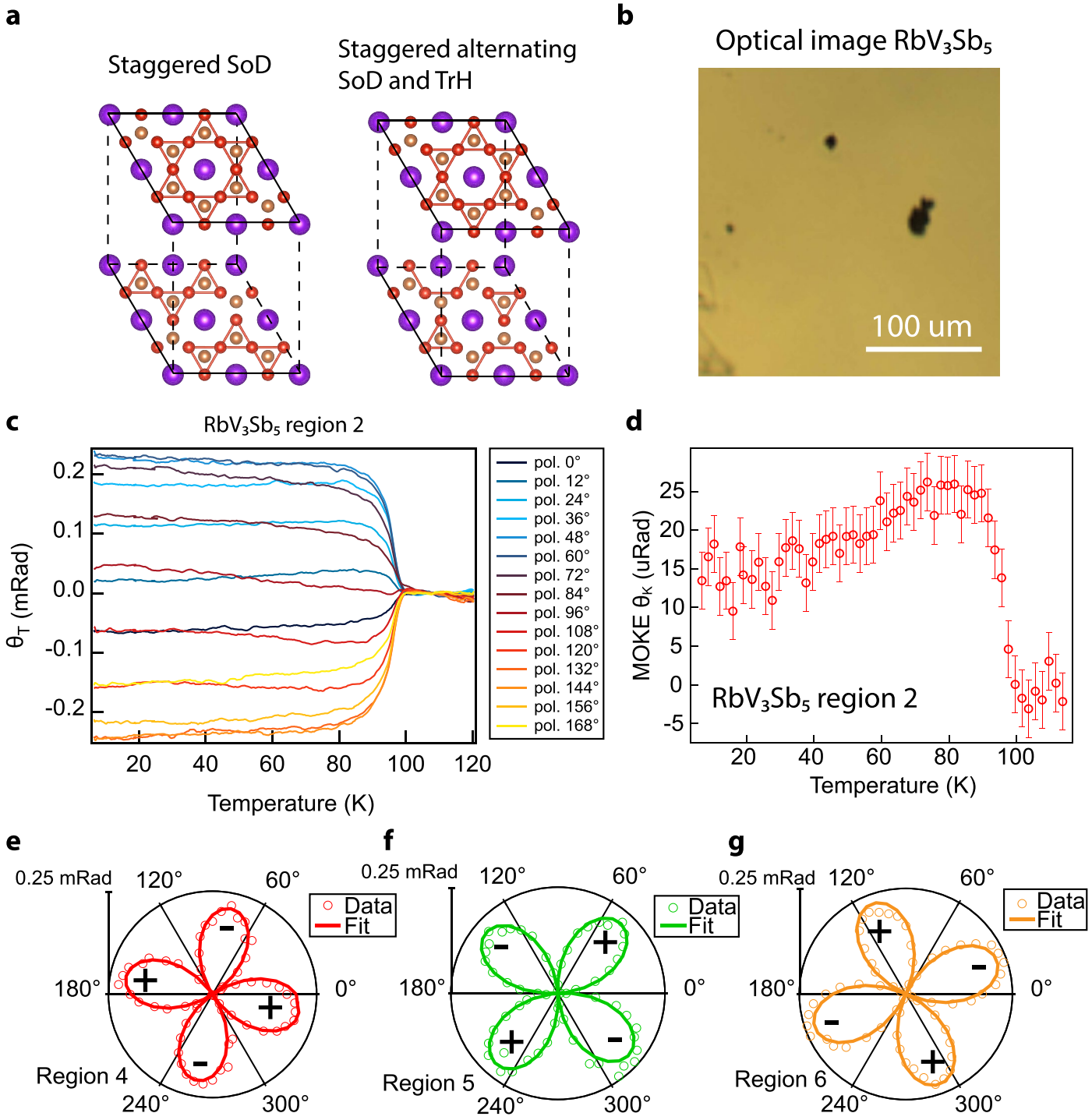

Extended Data Fig. 1 | Additional measurements on three-state nematic order and MOKE in RbV_3Sb_5. **a**, 3D lattice structures showing two other possible staggered CDW orders with a π phase shift, the staggered star-of-David (SoD) and the staggered alternating star-of-David (SoD) and tri-hexgonal (TrH) CDW orders. **b**, Optical image of the mapping region in Fig. 1(f) in RbV_3Sb_5. The black dots indicate impurities on the surface. **c**, θ_T vs temperature for various incident polarization measured in region 2 in RbV_3Sb_5. **d**, MOKE signal vs temperature measured at the zero birefringence incident angle in region 2 in RbV_3Sb_5. The error bar is 3.7 μRad (see main text for definition of error). **e**–**g**, Polar plots of the birefringence patterns at T = 70 K measured at the corresponding spots in region 4, 5 and 6 (see Fig. 1(f)), respectively.

https://doi.org/10.1038/s41567-022-01805-7

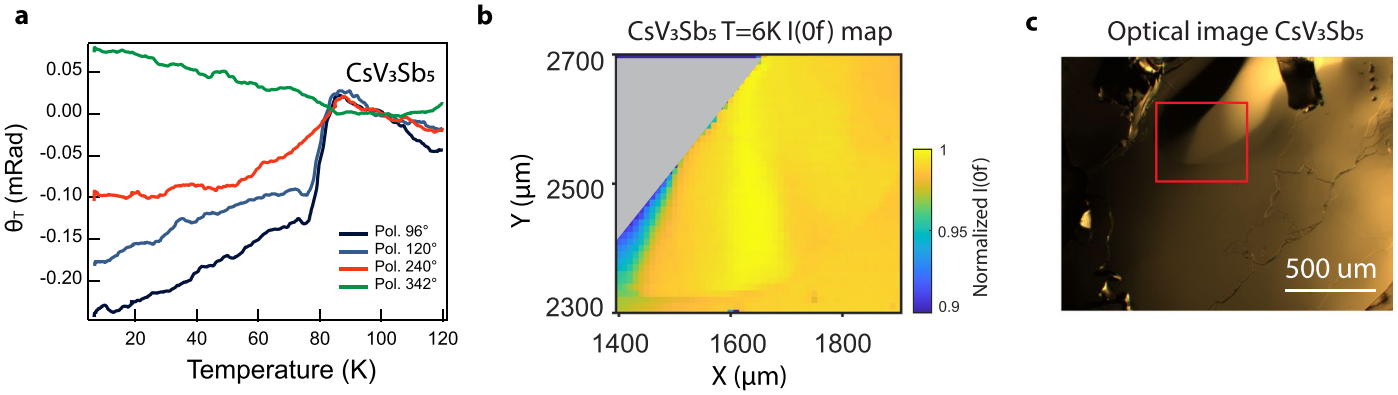

Extended Data Fig. 2 | θ_T vs temperature and characterization of the Cs sample in the main text. a, θ_T vs temperature for various incident polarization for the Cs sample shown in **b**,**c** in this figure, which is also the same sample for Fig. 2-4 in the main text and Extended data Fig.6-8. The sharp transition in θ_T at certain polarization is more consistent with a first order transition in the Cs sample, which is consistent with NMR/NQR measurements. Note that the Cs sample in extended data Fig.3 is a different sample, which shows a smoother transition. **b**, Mapping of the normalized I(0f) signal, the reflectivity, in the CsV_3Sb_5 sample. A variation of the I(0f) signal is observed in the mapping data, which indicates an uneven surface. **c**, Optical image of the cleaved Cs sample, the red box indicates the mapping region in **b**.

https://doi.org/10.1038/s41567-022-01805-7

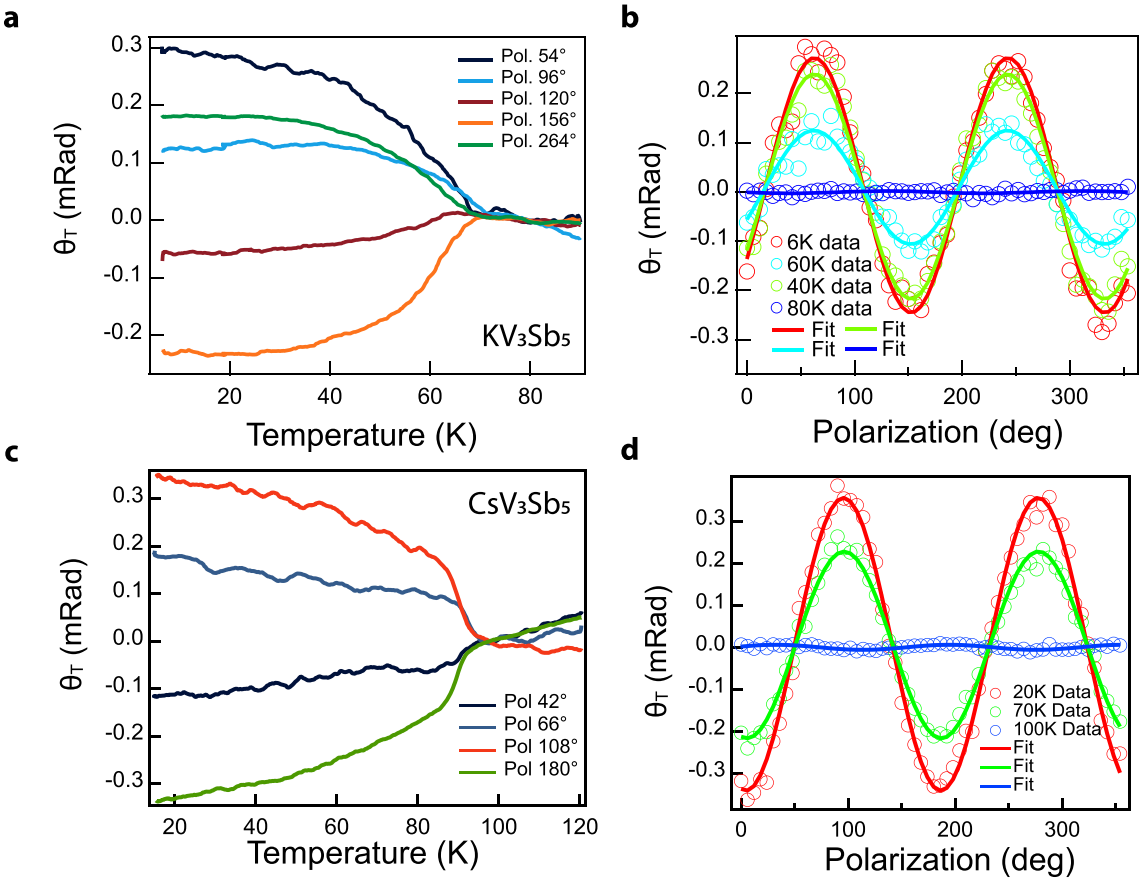

Extended Data Fig. 3 | Dependence of θ_T on temperature and incident polarization of K and Cs compound. a,**c**, θ_T vs temperature for various incident polarization for KV_3Sb_5 and CsV_3Sb_5, respectively. **b**,**d**, θ_T vs incident polarization at different temperature cuts for KV_3Sb_5 and CsV_3Sb_5, respectively.

https://doi.org/10.1038/s41567-022-01805-7

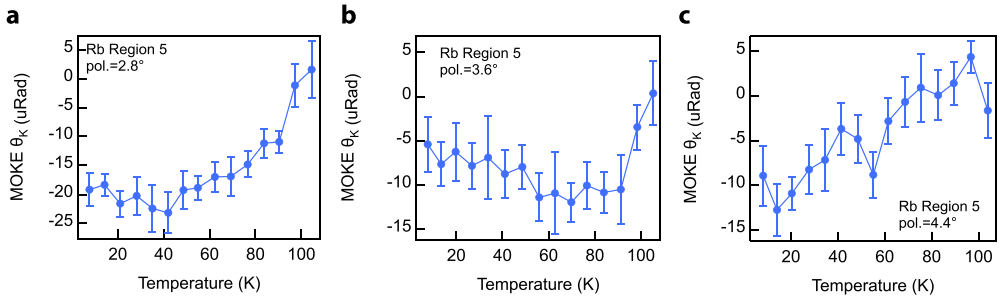

Extended Data Fig. 4 | Temperature dependent MOKE at ϕ_0 and $\phi_0 \pm 0.8$. a–**c**, MOKE signal measured at the incident angles $\phi_0 = 3.6^\circ$ and $\phi_0 \pm 0.8$ in region 5 for RbV_3Sb_5, where ϕ_0 is the incident angle that birefringence contribution is zero. The error bar is defined as the statistical error for data points averaged together over 2 K range bins.

https://doi.org/10.1038/s41567-022-01805-7

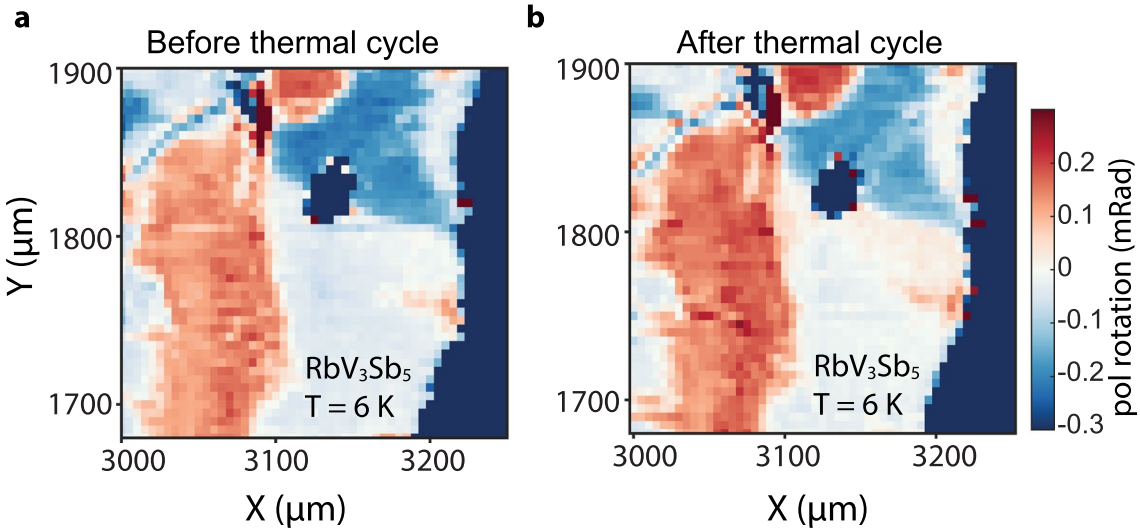

Extended Data Fig. 5 | Birefringence domains under thermal cycles. a,**b**, Spatial mapping of θ_f at T = 6 K, before and after thermal cycles for RbV_3Sb_5.

https://doi.org/10.1038/s41567-022-01805-7

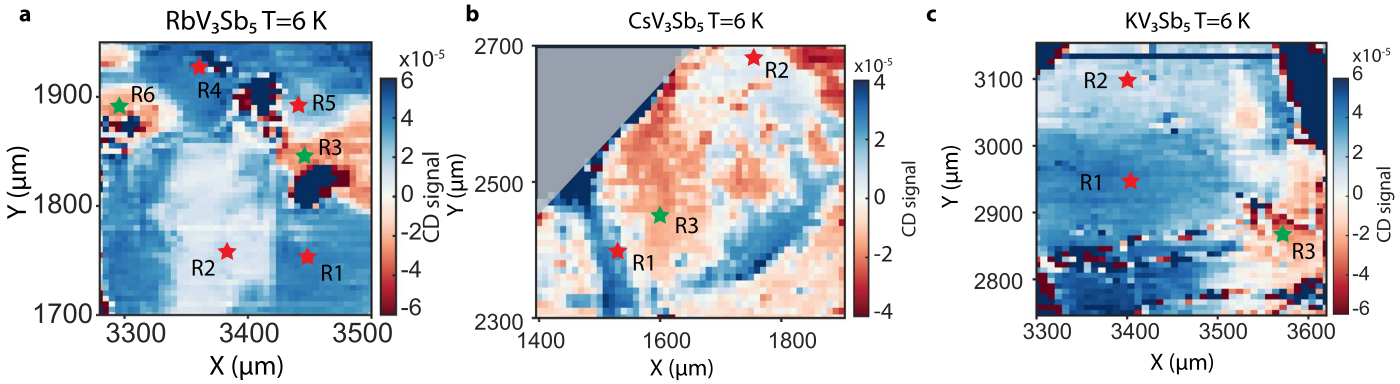

Extended Data Fig. 6 | Circular dichroism maps of AV_3Sb_5. a–c, Circular dichroism maps at T= 6 K for Rb, Cs and K compounds, respectively. The red and green star symbols indicate the positions where circular dichroism vs temperature measurements are performed in Fig. 4.

https://doi.org/10.1038/s41567-022-01805-7

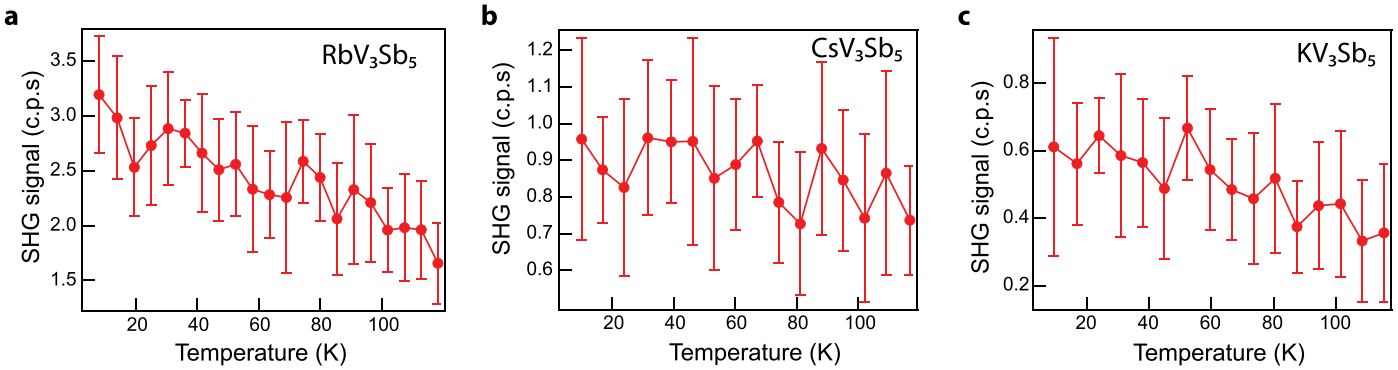

Extended Data Fig. 7 | Second harmonic generation of AV_3Sb_5. a–c, Second harmonic generation vs temperature for Rb, Cs and K compounds, respectively. The error bar is defined as the statistical error for data points averaged together over 5 K range bins.

https://doi.org/10.1038/s41567-022-01805-7

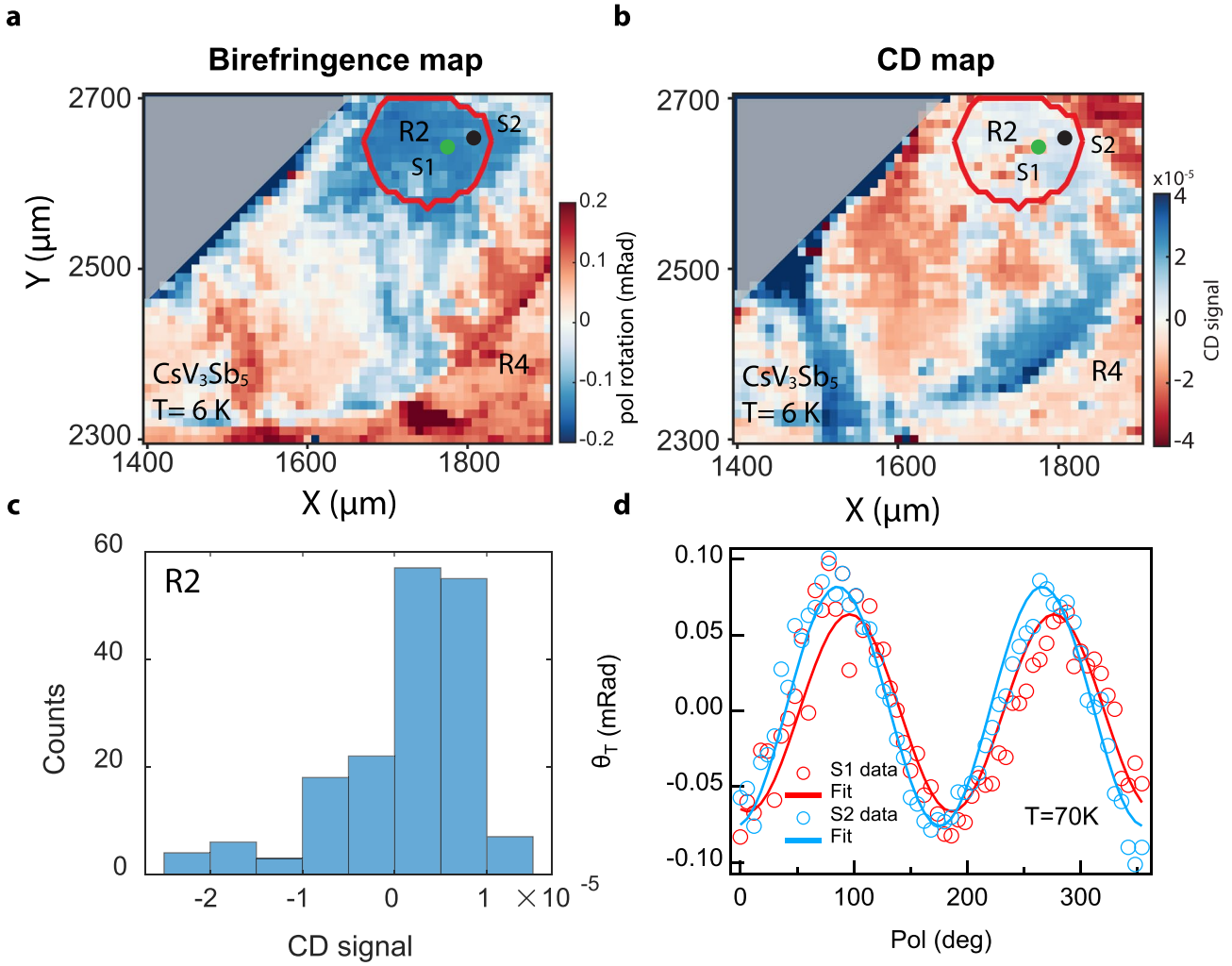

Extended Data Fig. 8 | Comparison of birefringence and circular dichroism maps of CsV3Sb5. a,**b**, The spatial birefringence and circular dichroism maps of CsV_3Sb_5 at T = 6 K, respectively. The region circled by red is region 2, where points within each region have the same birefringence pattern. The green and black dots indicate two spots in R2 (S1 and S2), which have same birefringence patterns but opposite signs of CD signal. **c**, Histograms of circular dichroism signals within region 2. Both positive and negative CD signals exist within R2. **d**, θ_T vs incident polarization at T= 70 K measured at S1 and S2 within R2, respectively.

https://doi.org/10.1038/s41567-022-01805-7

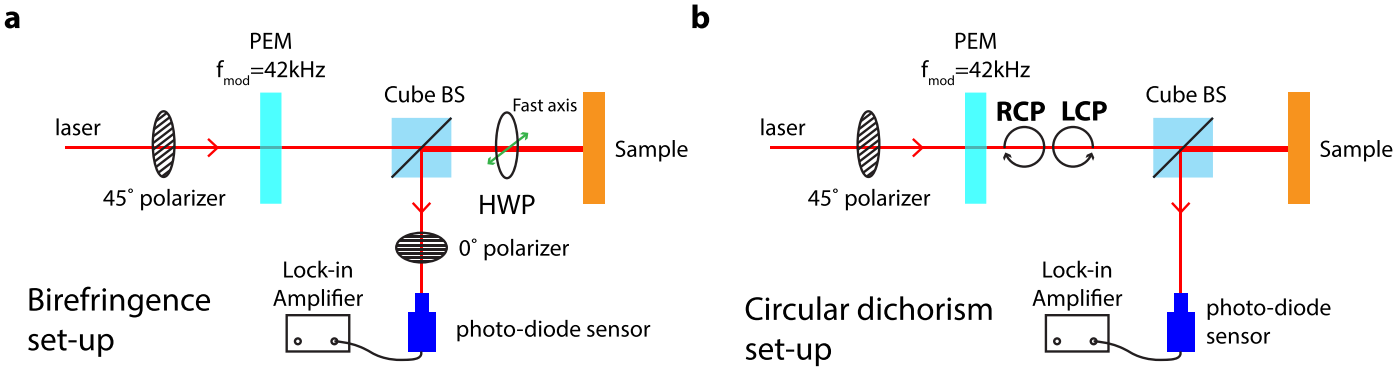

Extended Data Fig. 9 | Optical set-ups in this paper. a,**b**, Optical set-ups for the birefringence (**a**) and circular dichroism (**b**) measurements.